Carbohydrate Polymers 367 (2025) 123964

Contents lists available at ScienceDirect

Carbohydrate Polymers

journal homepage: www.elsevier.com/locate/carbpol

Molecular modeling of group B *Streptococcus* type II and III capsular polysaccharides explains low filter retention of type II and lack of cross-reactivity with type III

Nicole I. Richardson [a], Francesco Berti [c], Neil Ravenscroft [b], Michelle M. Kuttel [a,*]

[a] Department of Computer Science, University of Cape Town, Cape Town 7701, South Africa
[b] Department of Chemistry, University of Cape Town, Cape Town 7701, South Africa
[c] GSK, Via Fiorentina 1, 53100 Siena, Italy

ARTICLE INFO

Keywords:
Capsular polysaccharide
Carbohydrate epitopes
Conformation
Cross-protection
Group B *Streptococcus*
Molecular modeling
Vaccine processing

ABSTRACT

Group B *Streptococcus* (GBS) is a bacterial pathogen associated with significant morbidity and mortality in pregnant women and infants, particularly in resource-limited settings. A hexavalent vaccine candidate in development incorporates the capsular polysaccharides (CPSs) from the most prevalent serotypes: Ia, Ib, II, III, IV, and V.

Vaccine production is facilitated by a standardized CPS purification process. In the final purification step, a 30 kDa membrane filter gives high-yield recovery for five of the six CPSs, but <50 % for type II (GBSII), despite similar CPS structure and size. However, a smaller 10 kDa membrane improves recovery to about 90 %, suggesting that CPS conformation affects retention.

Here comparative molecular modeling – corroborated by through-space NMR correlations – reveals that GBSII forms compact, globular conformations, while type III (GBSIII) forms an elongated zig-zag. This explains GBSII's poor retention during filtration: GBSII's compact globules pass through the 30 kDa membrane more easily than GBSIII's elongated forms. Additionally, we identify distinct epitopes and compare their interactions with a GBSIII-specific fragment antibody to clarify the lack of cross-reactivity between GBSII and GBSIII. This work provides valuable mechanistic insight into physically observed behavior to inform development of multivalent GBS vaccines to reduce maternal and infant mortality.

1. Introduction

The bacterium *Streptococcus agalactiae*, commonly known as Group B *Streptococcus* (GBS), is a major cause of morbidity and mortality in pregnant women and infants globally (Dangor et al., 2023; Edmond et al., 2012; Gonçalves et al., 2022; Raabe & Shane, 2019). Although antibiotic treatment has some efficacy in treating GBS disease and preventing transmission, case fatality remains high and increasing antibiotic resistance (AMR) is a growing concern (Hayes et al., 2020; WHO Bacterial Priority Pathogens List, 2024: bacterial pathogens of public health importance to guide research, development and strategies to prevent and control antimicrobial resistance, 2024). Further, disease in non-pregnant adults is on the rise (Navarro-Torné et al., 2021). This has earned GBS recognition as a priority pathogen for the World Health Organization (WHO), both for the development of strategies to prevent and control AMR and as part of their "Defeating Meningitis by 2030 roadmap" (Defeating meningitis by 2030: a global road map, 2021).

Based on the capsular polysaccharide (CPS), GBS has ten serologically distinct serotypes: Ia, Ib, II, III, IV, V, VI, VII, VIII, and IX (Table 1) (Raabe & Shane, 2019). In infants, types Ia, Ib, II, III, IV, and V account for >85 % of isolated serotypes, with type III (GBSIII) the most prevalent, accounting for around half of the disease burden (Edmond et al., 2012; Raabe & Shane, 2019). In adults, type V appears most prevalent, with type II (GBSII) also associated with a significant disease burden (Navarro-Torné et al., 2021; Raabe & Shane, 2019).

A vaccine targeting the six main GBS serotypes is expected to have a significant positive impact on disease burden and, after several decades of development, clinical trials for maternally administered GBS vaccines

* Corresponding author.
E-mail addresses: nicole.richardson@uct.ac.za (N.I. Richardson), francesco.x.berti@gsk.com (F. Berti), neil.ravenscroft@uct.ac.za (N. Ravenscroft), mkuttel@cs.uct.ac.za (M.M. Kuttel).

https://doi.org/10.1016/j.carbpol.2025.123964
Received 14 March 2025; Received in revised form 20 June 2025; Accepted 25 June 2025
Available online 27 June 2025

Table 1
Line structures of the ten GBS serotypes (Berti et al., 2014; Pinto & Berti, 2014). Side chains are indicated in bold with square brackets.

Type	Line Structure
Ia	→4) **[αDNeu5Ac(2→3)βDGal(1→4)βDGlcNAc(1→ 3)]** βDGal(1→4)βDGlc (1→
Ib	→4) **[αDNeu5Ac(2→3)βDGal(1→3)βDGlcNAc(1→ 3)]** βDGal(1→4)βDGlc (1→
II	→3)βDGlc(1→2) **[αDNeu5Ac(2→3)]** βDGal(1→4)βDGlcNAc(1→3) **[βDGal (1→6)]** βDGal(1→4)βDGlc(1→
III	→3)βDGal(1→4)βDGlc(1→6) **[αDNeu5Ac(2→3)βDGal(1→4)]** βDGlcNAc(1→
IV	→4)αDGlc(1→4) **[αDNeu5Ac(2→3)βDGal(1→4)βDGlcNAc(1→6)]** βDGal (1→4)βDGlc(1→
V	→4) **[αDNeu5Ac(2→3)βDGal(1→4)βDGlcNAc(1→6)]** αDGlc(1→4) **[βDGlc (1→3)]** βDGal(1→4)βDGlc(1→
VI	→6) **[αDNeu5Ac(2→3)βDGal(1→3)]** βDGlc(1→3) βDGal(1→4) βDGlc(1→
VII	→4) **[αDNeu5Ac(2→3)βDGal(1→4)βDGlcNAc(1→6)]** αDGlc(1→4)βDGal (1→4)βDGlc(1→
VIII	→4) **[αDNeu5Ac(2→3)]** βDGal(1→4)βLRha(1→4)βDGlc(1→
IX	→4) **[αDNeu5Ac(2→3) βDGal(1→4)βDGlcNAc(1→6)]** βDGlcNAc(1→4)β DGal(1→4)βDGlc(1→

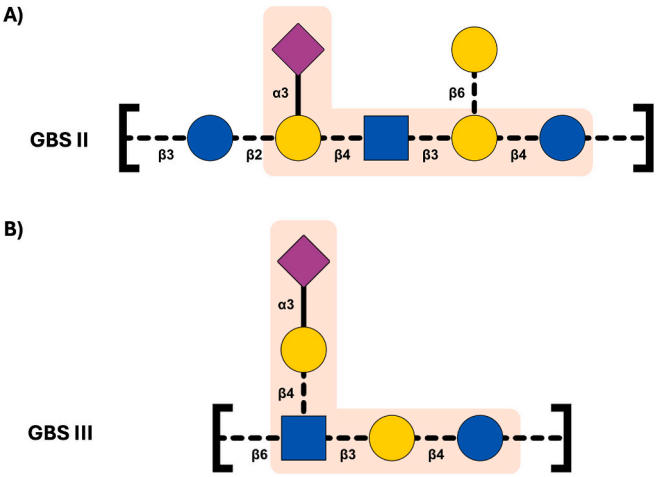

Fig. 1. Repeating unit structures for **A)** Group B Streptococcus type II (GBSII) and **B)** Group B Streptococcus type III (GBSIII) capsular polysaccharides (CPS) represented with the Symbol Nomenclature for Glycans (SNFG) symbols (Neelamegham et al., 2019; Varki et al., 2015). Glucose residues are blue circles, galactose yellow circles, N-Acetyl glucosamine blue squares, and sialic acid purple diamonds. The common structural motif for the CPSs is indicated by background shading.

are in advanced stages. The leading vaccine candidate is a hexavalent glycoconjugate formulation produced by Pfizer, comprising types Ia, Ib, II, III, IV, and V chemically attached to the CRM_{197} carrier protein; other glycoconjugate and protein vaccines are also in development (Bjerkhaug et al., 2023). The Pfizer vaccine candidate is predicted to prevent 75 to 95 % of disease, significantly reducing mortality and providing considerable benefit in terms of reduced morbidity and healthcare costs (Madhi et al., 2023; Procter et al., 2023). Thus far, clinical trials show promising safety and efficacy profiles and, thanks to the precedents set in maternal vaccine acceptance during the COVID-19 pandemic, a commercially available vaccine may be available before another decade passes (Baker, 2023; Bjerkhaug et al., 2023).

The first step in glycoconjugate vaccine production is development of a high-yielding process to prepare purified polysaccharide (Hennessey Jr et al., 2018). Efficient preparation of a multivalent vaccine against multiple serotypes is facilitated by the application of standard procedures to achieve this, using a variety of precipitation, chromatographic and/or filtration steps. GSK (formerly Novartis Vaccines) reported that the final filtration step in purification of their GBS CPSs is conducted with a 30 kDa molecular weight cutoff (MWCO) membrane (Costantino et al., 2015). Surprisingly, when applied to GBSII CPS, yields were <50 %, unlike those obtained for serotypes Ia, Ib, III and V (Berti et al., 2016). This was despite GBSII having a similar structure and molecular weight to the comparator GBSIII. Replacing the 30 kDa membrane with a smaller pore 10 kDa membrane yielded about 90 % recoveries for GBSII. Berti et al. hypothesized that the GBSII CPS has a more linear "pencil-like" conformation than GBSIII, which reduces the hydrodynamic radius, resulting in poor retention by the 30 kDa membrane (Berti et al., 2016). However, this theory is at odds with the ratio of radius of gyration to hydrodynamic radius (Rg/Rh) of 1.13 for GBSII, which suggests a polymeric conformation between a random coil (Rg/Rh ~ 1.5) and a homogeneous (hard) sphere (Rg/Rh ~ 0.77) rather than a linear chain (Rg/Rh ~ 2) (Burchard, 2003; Costantino et al., 2015).

Seven of the ten GBS CPS repeating units (RUs) contain the same four monosaccharides (Table 1): *β*-D-glucose (*β*Glc), *β*-D-galactose (Gal), *N*-Acetyl-*β*-D-glucosamine (GlcNAc) and a side chain terminating in *N*-Acetyl-*α*-D-neuraminic acid (Neu5Ac, sialic acid), albeit in different molar ratios and with varying structural organization. (Berti et al., 2014; Pinto & Berti, 2014). Type IV and VII have an additional *α*-D-glucose (*α*Glc) and Type VIII replaces GlcNAc with *β*-L-rhamnose (Rha). Unlike pathogens such as *Streptococcus pneumoniae* (Feemster et al., 2024), the structural similarities in the CPS's do not result in cross-protection between heterogenous serotypes in humans (Baker & Kasper, 1985); this suggests significant conformational differences between all the GBS serotypes. This has been demonstrated for serotypes 1a and 1b: although this pair differs only in a single linkage in a side chain, they are antigenically distinct (Schifferle et al., 1985), likely arising from a significant difference in side chain orientation shown by modeling studies (Del Bino et al., 2019).

In this study, we hypothesize that conformational comparison of GBSII (Fig. 1A) with GBSIII (Fig. 1B) will provide a conformational rationale for both the poor retention of GBSII during filtration and the lack of cross-reactivity (Baker & Kasper, 1985) between the serotypes. GBSIII is the most prevalent and widely studied serotype, comprising a pentasaccharide RU with a trisaccharide backbone with a highly flexible 1→6 linkage and a disaccharide side chain (Neu5Ac(2→3) Gal). Our prior simulations of 6 RUs of the GBSIII CPS showed a flexible molecule with a "zig-zag" backbone conformation and side chains exposed at the bends (Kuttel & Ravenscroft, 2019). GBSII is also targeted for vaccine inclusion and shares some structural similarity with GBSIII (Fig. 1, orange shaded regions), but has a longer, heptasaccharide RU with a pentasaccharide backbone and two monosaccharide side chains: Neu5Ac and Gal. No conformational studies of GBSII have been published to date.

Studies show no cross-reactivity in humans between GBSII and GBSIII (Baker et al., 2003). For both, two main classes of functional antibody are observed: a major, sialic acid dependent population, and a minor sialic acid independent (galactose dependent) population; the former primarily recognizes the native CPS and the latter both the native CPS and desialylated CPS (Carboni et al., 2017; Kasper et al., 1983). For GBSIII, a fragment antibody (FAb) bound to a 2 RU CPS fragment (DP2) confirmed the importance of the sialic acid moiety in antibody binding (Carboni et al., 2017).

We employ molecular dynamics simulations to compare the conformation and dynamics of the GBSII CPS to the GBSIII CPS; where possible using through space correlations from 1D and 2D NMR experiments to validate the conformations from the modeling. This extends our previous work modeling GBSIII molecules to longer oligosaccharides and provides the first simulations of GBSII molecules. Our aims are: to provide a mechanistic rationale for observed differing filtration behavior from conformational differences in the GBSII and GBSIII molecules; to probe the effect of RU length on CPS conformation for both GBSIII and GBSII; and to rationalize the lack of cross-reactivity between GBSII and GBSIII by comparing potential binding epitopes presented by the two antigens as well as their potential for binding a GBSIII fragment

antibody as orthogonal validation.

2. Materials and methods

Chain length is an important consideration when modeling CPSs, as short chains may have insufficient molecular flexibility, while long chains are more computationally expensive to model. Typically, we perform modeling of shorter 3 and 6 RU chains, which are considered sufficient to explore potential antibody binding epitopes (Kabat, 1966; Nonne et al., 2024). Indeed, for GBSIII it has been shown that 1–2 RU is sufficient for antibody binding (Carboni & Adamo, 2020; Carboni et al., 2017). In this investigation, however, longer chains were required to evaluate secondary structures and conformational dynamics.

This study compares GBSIII with a five residue repeat unit CPS (three backbone residues per RU) with GBSII with a seven residue repeat unit CPS (five backbone residues per RU). For comparison purposes, we considered molecules of the same length backbone and simulated five oligosaccharides in total (two for GBSIII and three for GBSII): GBSII 6 RU and GBSIII 10 RU (each a 30 residue backbone); GBSII 9 RU and GBSIII 15 RU (45 residue backbones); and an additional 12 RU GBSII chain (60 residue backbone). For the latter, the corresponding GBSIII 20 RU system was deemed too computationally expensive to run for this work.

2.1. Molecular dynamics

The CPS chains were built as protein data bank (PDB) files using the CarbBuilder software (version 1.2.45) (Kuttel et al., 2011; Kuttel et al., 2016) and visualized with the Visual Molecular Dynamics (VMD) software (Humphrey et al., 1996). Starting structures for each molecule were built using low energy glycosidic linkages from potential of mean force calculations, as per our prior work (Richardson et al., 2021) (see Supplementary Fig. 1) and the psfgen tool was used by CarbBuilder to create protein structure files (PSF) for simulation with the CHARMM36 additive force field used to model the carbohydrates (Guvench & MacKerell, 2008; Guvench & MacKerell Jr, 2009). The starting structures were subsequently minimized with the Nanoscale Molecular Dynamics (NAMD) (Phillips et al., 2020) software (version 2.14 for the 6 RU and version 3.0 for the longer RU chains) for 10,000 steps at 300 K. Minimized structures were solvated using VMD's built in solvation and ionization tools to create cubic TIP3P (Jorgensen et al., 1983) water boxes of side length: 90 Å for the 6 RU GBSII; 100 Å for the 9 RU GBSII; 140 Å for the 12 RU GBSII and 10 RU GBSIII; and an orthorhombic 120 × 130 × 120 Å box for the 15 RU GBSIII system. Systems were then ionized with one sodium (Na^+) counter ion per repeating unit for charge neutrality. Initial minimization and heating protocols comprised 5 K incremental temperature reassignments from 10 K to 300 K,with 500 steps of NAMD minimization and 8000 steps of MD at each temperature reassignment. Solvated and ionized structures (PDB and PSF files) for each system are available as Supplementary Information.

The 6 RU simulation was run using NAMD (version 2.13) with CUDA extensions for graphics processor acceleration; simulations of 10 RU and 12 RU were run using NAMD (version 3.0) with CUDA extensions for graphics processor acceleration and a GPU resident computational mode (Phillips et al., 2020).

Periodic boundary conditions equivalent to the cubic box size were employed for the solvated simulation with wrapping on. Long range electrostatics were implemented with the Particle Mesh Ewald summation grid spacing set to 1 (Darden et al., 1993). Atoms were not held fixed, and the initial center of mass motion was turned off. The 1–3 pairs were excluded from non-bonded interactions, 1–4 interactions were not scaled, and the dielectric constant was set to 1. Smoothing functions were applied to both the electrostatic and van der Waals forces, with switching and cut-off distances of 12 Å and 15 Å for 6 RU chains and 10 Å and 12 Å for 10 RU and 12 RU chains, respectively.

A Leap-Frog Verlet integrator was used to integrate the equations of motion over a step size of 1 fs. A distance of 18 Å was used as the cut-off for inclusion in the pair list for calculation of non-bonded forces for 6 RU simulations and 15 Å for 10 and 12 RU simulations. The short-range non-bonded interactions were calculated every 1 fs, full electrostatics calculations were performed every 2 fs, and atoms were reassigned every 10 fs (Van Gunsteren & Berendsen, 1988).

Simulations were sampled under the isothermal-isobaric (nPT) ensemble. Langevin dynamics (Feller et al., 1995) were used to control the temperature with a damping coefficient of 5/ps. Nosé-Hoover Langevin piston dynamics were used as a barostat to maintain a target pressure of 1 atm (Hoover, 1985; Nosé & Klein, 1983). Variable system volume was used with a piston period of 100 fs and decay of 50 fs.

Simulations of 2500 ns were performed for all the molecules modeled, except for GBSII 6 RU (2000 ns). The simulation length comprised 200–500 ns of equilibration (GBSII 6 and 9 RU, 200 ns; GBSII 12 RU, 500 ns; GBSIII 10 RU 400 ns; GBSIII 15 RU, 200 ns) and 1800–2300 ns of production run as was required for convergence.

2.2. Data analysis

Trajectories were extracted at 25 ps intervals, with analysis performed on frames 250 ps apart. Metrics such as end-to-end distances were extracted from the simulation trajectories using Tcl scripting via VMD's Tk console. Data analyses were performed with in-house Python scripts and plots generated using Matplotlib (Hunter, 2007).

Molecular conformations were visualized using VMD with the Licorice or VDW molecular representations; when required, the PaperChain visualization algorithm was used to highlight carbohydrate rings (Cross et al., 2009) and the Quicksurf visualization algorithm for surfaces (Krone et al., 2012).

The previously generated 1000 ns of simulation data for GBSIII 6 RU (200 ns of equilibration 800 ns of production run) (Kuttel & Ravenscroft, 2019) was reanalyzed in line with the new data (Supplementary Fig. 2).

2.2.1. Convergence

We addressed convergence using block standard averaging (Grossfield & Zuckerman, 2009) applied to two metrics: end-to-end distance and radius of gyration (Supplementary Fig. 3). Block standard averaging was implemented with in-house Python scripts.

For all simulations, the blocked standard error (BSE) reached plateaus for both metrics, indicating convergence. The simulation lengths were large multiples of the correlation times for end-to-end distance (GBSII 6 RU, 46 ns; GBSII 9 RU, 49 ns; GBSII 12 RU, 38 ns; GBSIII 10 RU, 57 ns; GBSIII 15 RU, 68 ns) and radius of gyration (GBSII 6 RU, 63 ns; GBSII 9 RU, 146 ns; GBSII 12 RU, 126 ns; GBSIII 10 RU, 114 ns; GBSIII 15 RU, 66 ns). Further, the numbers of independent samples were $>>1$ for both the end-to-end distance (GBSII 6 RU, 39; GBSII 9 RU, 47 ns; GBSII 12 RU, 53; GBSIII 10 RU, 37; GBSIII 15 RU, 34 ns) and the radius of gyration (GBSII 6 RU, 28; GBSII 9 RU, 16 ns; GBSII 12 RU, 16; GBSIII 10 RU, 18; GBSIII 15 RU, 35 ns). Our designated equilibration times of 200–500 ns are therefore greater than the correlation time and the simulations all appeared converged.

2.2.2. Chain extension and conformations

The end-to-end distance, *r*, was measured from C1 of Gal at the non-reducing end, to C2 of Gal for GBSII or C3 of Gal for GBSIII at the reducing end, thus excluding the highly flexible terminal residues.

Clustering analysis of the simulation trajectory involves grouping frames that are conformationally similar to give the preferred conformations adopted by the molecule. The most common chain conformations for each simulation were determined by clustering the production trajectory frames into families and calculating the relative occupancies of each family. Clusters comprising <6 % of the production run (post equilibration) were discarded. Clustering was performed using the WMC PhysBio plug-in for VMD's built-in measure cluster command (Luis, 2012). Prior to clustering, the GBSII molecules were aligned (excluding the *N*-acetyl and O6/C6 moieties) as follows: GBSII 6 RU on the atoms of

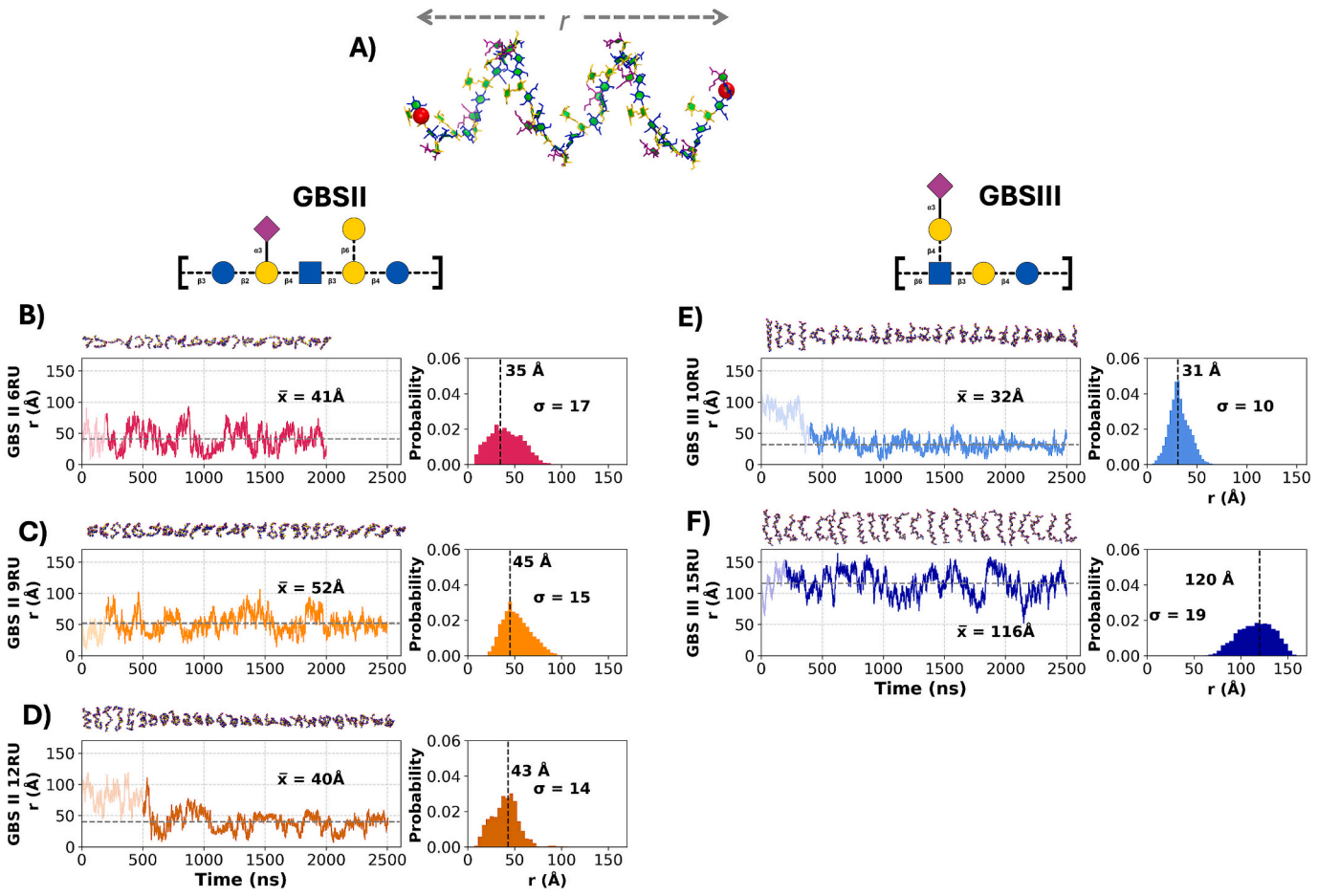

Fig. 2. **A)** End-to-end distance, r, indicated on the 12 RU GBSII molecule. Simulation time series graphs of r (left) and corresponding histograms (right) are shown for: **B)** GBSII 6 RU (pink); **C)** GBSII 9 RU (orange); **D)** GBSII 12 RU (light brown); **E)** GBSIII 10 RU (light blue); and **F)** GBSIII 15 RU (dark blue). Small conformational snapshots at 100 ns intervals are shown above the time series plots. Translucent regions in the time series plots indicate the equilibration period; dashed horizontal lines indicate the average value of r ($\bar{x}$). The histograms are labeled with the standard deviations (σ) and modal peak values indicated with vertical dashed lines. The repeating unit structures for GBSII and GBSIII are shown above their respective plots and, where applicable, molecules are shown in VMD's Licorice, PaperChain (Cross et al., 2009), or VDW visualization styles using SNFG colors.

RU 3 (residue order as shown in Table 1) as well as βGlc and Gal residues of RU 4; GBSII 9 RU on the atoms of RU 3, 4, 5, 6 molecules; GBSII 12 RU on the atoms of RU 6, 7, 8, 9 molecules. Clustering was performed as an RMSD fit using ring and linkage atoms of: RU 2–5 for GBSII 6 RU (cutoff 8 Å); RU 2–8 for GBSII 9 RU (cutoff 10 Å); RU 2–11 for GBSII 12 RU (cutoff 12 Å). For GBSIII, alignment was performed on the ring atoms of the GlcNAc residues of RU 3–8 for GBSIII 10 RU and RU 3–13 for GBSIII 15 RU. Clustering was performed on the ring and linkage atoms of RU 2–9 for GBSIII 10 RU (5 clusters, cutoff 8 Å); and RU 3–13 for GBSIII 15 RU (5 clusters, cutoff 10 Å).

Where applicable, hydrogen bonding was represented using the HBond visualization algorithm in VMD with a distance of 4 Å and an angle of 30°.

2.2.3. Glycosidic linkages

Given the limited flexibility of the carbohydrate ring, the primary source of flexibility in the repeating unit arises from the glycosidic linkages between neighboring monosaccharides. These glycosidic linkages are conveniently described by two dihedral angles, phi (ϕ) and psi (φ). As per our previous work, we define $\phi = H_1\text{-}C_1\text{-}O_1\text{-}C'_x$ and $\varphi = C_1\text{-}O_1\text{-}C'_x\text{-}H'_x$ with x representing the linkage position (Richardson et al., 2023). In the case of the (2➔3) linked Neu5Ac, these definitions were adjusted to $\phi = C_1\text{-}C_2\text{-}O_2\text{-}C'_3$ and $\varphi = C_2\text{-}O_2\text{-}C'_3\text{-}H'_3$. For the ➔6 linkages, which are comprised of three instead of two bonds, we define $\phi = H_1\text{-}C_1\text{-}O_1\text{-}C'_x$ and $\varphi = C_1\text{-}O_1\text{-}C'_6\text{-}C'_5$ and omega (ω) = $O_1\text{-}C'_6\text{-}C'_5\text{-}H'_5$. Analysis of glycosidic linkages is presented in the Supplementary Information (Supplementary Information Section 1 and Supplementary Fig. 4).

2.2.4. Molecular surface and volume analysis

The solvent accessible surface area (sasa) for each molecule was analyzed using VMD's built in "measure sasa" command with a large van der Waal's radius of 1.4 Å to represent the potential antibody accessible surface. An analysis of sasa for different probe sizes (1–20 Å) is presented in Supplementary Table 1 and Supplementary Fig. 5.

Volume was calculated using VMD's Mol_Volume tool (Balaeff Balaeff, 2006). This uses a method akin to a Monte Carlo method to estimate molecular volume by measuring how much of a predefined grid is occupied by the molecule's atoms. Van Der Waal's radii were obtained from (Mantina et al., 2009).

2.2.5. Fragment antibody complex

The PDB file describing the structure of a fragment antibody (FAb) of the rabbit monoclonal anti-PSIII NVS -1-19-5 antibody bound to a 2 RU (DP2) GBSIII CPS fragment was obtained from the official RSCB PDB (PDB ID: 5M63) (Carboni et al., 2017). The overlay of our CPS molecules with the FAb binding site were created by aligning residues of the bound DP2 and a 2 RU fragment of the 10 or 15 RU GBSIII molecules. The alignment used the Neu5Ac and Gal residues in the binding pocket as well as the adjacent βGlc, Gal and GlcNAc of the backbone. We used the representative frame of the primary cluster, as well as a representative

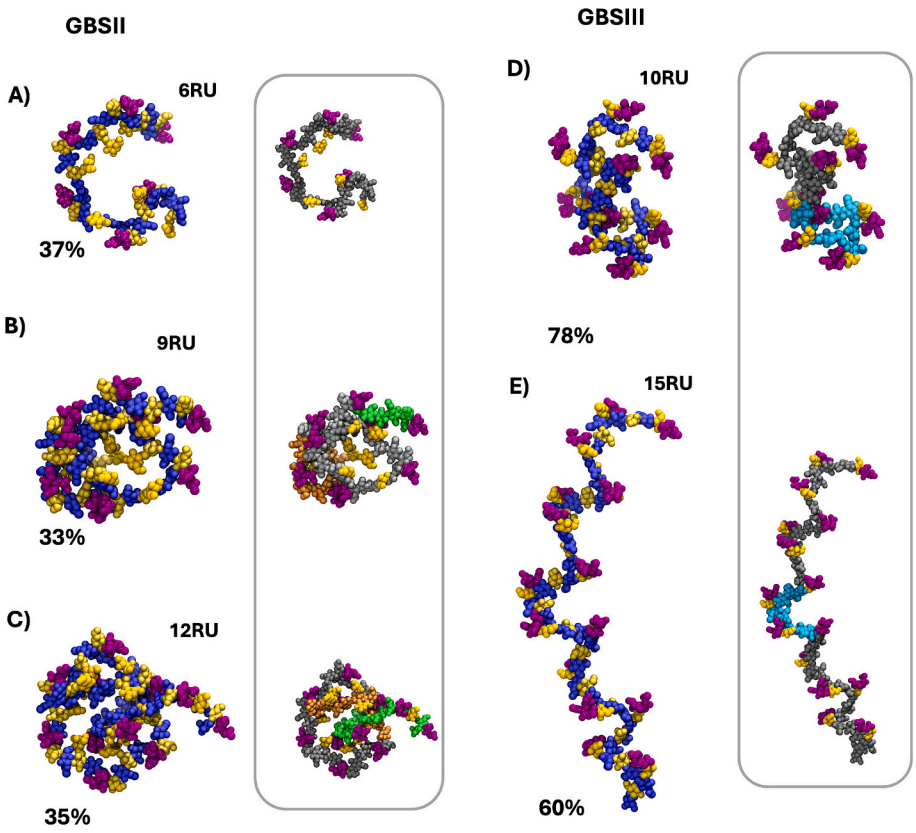

Fig. 3. Representative frames for the main conformational families identified for the modeled GBSII and GBSIII molecules: **A)** GBSII 6 RU, **B)** GBSII 9 RU, **C)** GBSII 12 RU **D)** GBSIII 10 RU; and **E)** GBSIII 15 RU. Cluster occupancies are indicated by percentage of trajectory frames belonging to that cluster and the primary clusters occurred regularly throughout the trajectory. Atoms are shown using VMD's VDW visualization style with residues colored according to SNFG colors: Neu5Ac - purple; βGlc - blue; βGal - yellow; βGlcNAc - blue. The inset box for GBSII shows: the molecule backbones (grey) and terminal RUs (green and orange) highlighting the pentagonal-ring shape formed by the central backbone RUs as well as side chain Neu5Ac (purple) and Gal (yellow) residues. The inset box for GBSIII shows the backbones of the molecules (grey) with side chains (purple and yellow) and bends in the backbone (cyan).

sample of frames (every 200th frame of the trajectory).

2.2.6. NMR analysis

The GBSII polysaccharide sample (10 mg) was lyophilized and exchanged twice with 99.9 % D_2O (Sigma Aldrich, Pty. Ltd., Johannesburg, South Africa), then dissolved in 600 μL of D_2O and introduced into a 5 mm NMR tube for data acquisition. 1D ^{1}H and ^{13}C and 2D, COSY, TOCSY, NOESY, HSQC, HMBC and hybrid HSQC-TOCSY and HSQC-NOESY spectra were obtained using a Bruker Avance III 600 MHz NMR spectrometer (Bruker BioSpin AG, Fällanden, Switzerland) equipped with a BBO Prodigy cryoprobe and processed using standard Bruker software (Topspin 3.2). The probe temperature was set at 343 K. 1D TOCSY experiments were performed using a mixing time of 200 ms. The 2D NOESY experiment was performed using mixing times of 300 and 500 ms and the 1D variants using mixing times of 300, 400 and 500 ms. 2D experiments were recorded using non-uniform sampling: 50 % for homonuclear experiments. Spectra were referenced relative to the H3ax/C3 signal of terminal Neu5Ac: ^{1}H at 1.79 ppm and ^{13}C at 40.68 ppm (Lundborg & Widmalm, 2011).

3. Results

We start our analysis with a comparison of the chain extension in the five oligosaccharides modeled (three for GBSII and two for GBSIII). This is followed by conformational analysis and an investigation of hydrogen bonding. Next, we explore the molecular surface and volume before considering potential antibody binding epitopes.

3.1. Chain extension

The fluctuation in molecular end-to-end distance, *r*, over the length of a simulation is commonly used as a measure of chain extension in carbohydrates and provides a high-level overview of the molecular behavior. Here we define *r* to exclude the mobile terminal residues and side chains where applicable (Fig. 2A). Fig. 2 shows the *r* times series plots and corresponding distributions over the 2000–2500 ns simulations for each of the five oligosaccharides modeled: GBSII (6, 9, 12 RU) and GBSIII (10, 15 RU). Molecules are ordered on backbone length, with the first row of GBSII 6 RU (Fig. 2B) and GBSIII 10 RU (Fig. 2E) corresponding to 30 backbone residues and the second row of GBSII 9 RU (Fig. 2C) and GBSIII 15 RU (Fig. 2F) corresponding to 45 residues. The final row corresponding to 60 residues contains only the GBSII 12 RU molecule (Fig. 2D), as the large water box required for a very elongated GBSIII 20 RU was too computationally expensive to run.

The end-to-end distance analysis for GBSII shows surprising results: despite the backbone length increasing from 30 residues (Fig. 2B) to 45 (Fig. 2C) and then 60 residues (Fig. 2D), the *r* distance for the three oligosaccharides is similar, with mean values ($\bar{x}$, dashed lines in Fig. 2) for *r* of $\bar{x} = 41$ Å for 6 RU, 52 Å for 9 RU and 40 Å for 12 RU. Further, comparison of the *r* distribution histograms shows that the standard deviation, σ, decreases with increasing chain length: 17 Å (6 RU) > 15 Å (9 RU) > 14 Å (12 RU). The reason for this is indicated by the conformational snapshots above the time series in Fig. 2, which show increasingly globular conformations as the chain length increases for GBSII. The 6 and 9 RU molecules (Fig. 2B and C) start in similar, short *r* conformations and proceed to oscillate between a variety of more and less extended, bent "C-shaped" conformations for the 6 RU molecule or,

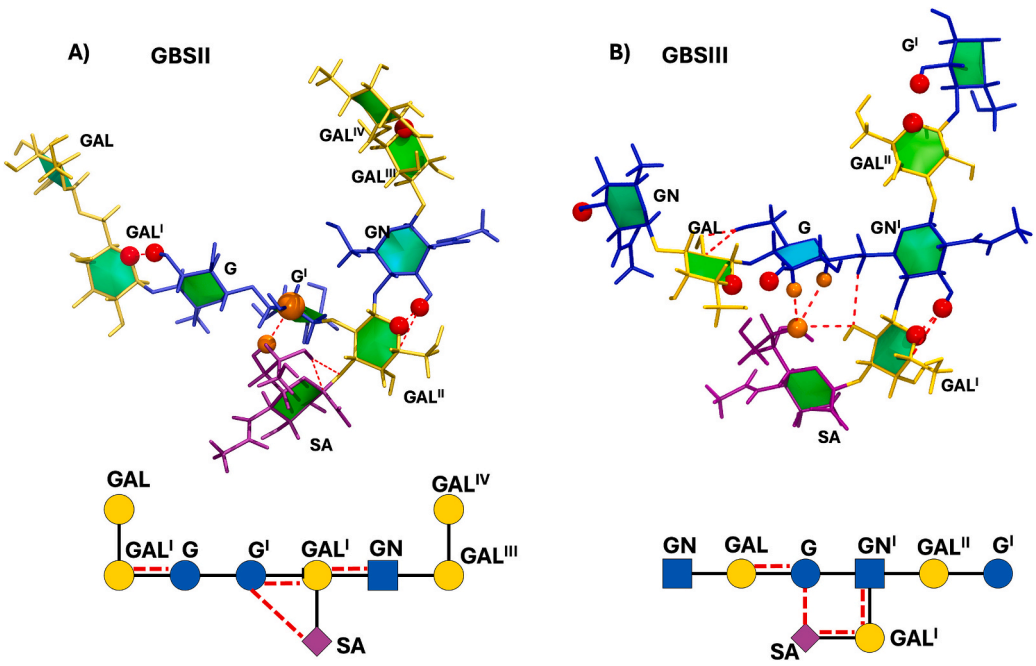

Fig. 4. Hydrogen bonding (dashed red lines) indicated on short molecular fragments equivalent to 1–2 RU of the CPS: **A)** GBSII 9 RU backbone and **B)** GBSIII 15 RU backbone. Molecules are shown in Licorice / PaperChain representations and hydrogen bonding is indicated by dashed red lines. Characteristic hydrogen bonds occur between the side chain Neu5Ac (SA) residues and backbone βGlc (G^{I}) indicated by orange spheres. Additional stabilizing hydrogen bonds occur between adjacent βGlc/GlcNAc HO3 and βDGal O5 residues are indicated by red spheres. Schematics of the molecules are shown in SNFG below the corresponding molecules and residues are labeled with colors as follows: SA – Neu5Ac (purple); G – βGlc (blue); GAL – Gal (yellow); GN – GlcNAc (blue).

highly folded/ collapsed conformations and slightly more extended "cobra-like" conformations for the 9RU. Conversely, the longer 12 RU molecule (Fig. 2D) starts in a longer *r* conformation and while initially more extended, quickly shifts to a highly collapsed, globular conformation which is sustained for most of the simulation.

In comparison, the GBSIII molecules have the opposite trend: *r* increases with increasing chain length, as is usually expected. The mean end-to-end distances are $\overline{x} = 32$ Å (10 RU, Fig. 2E) and 116 Å (15, Fig. 2F). Similarly, standard deviation, σ, increases with increasing chain length of the GBSII molecules: from $\sigma = 10$ Å (10 RU) to $\sigma = 19$ Å (15 RU). The conformational snapshots show some collapse for the 10 RU molecule, but a very extended chain for the 15RU. The 10 and 15 RU molecules (Fig. 2E and F) begin in a very extended zig-zag conformations with high *r* values. The 10 RU molecule quickly shifts to shorter *r* values for the remainer of the simulation, which correspond to zig-zag conformations with a highly conserved fold at one end of the backbone. The 15 RU molecule, however, remains in the extended conformation throughout with slight bend in the middle of the backbone, creating a gentle curve.

3.2. Chain conformations

As predicted by the *r* analysis above, there are significant differences between the primary conformational families of GBSII and GBSIII (Fig. 3, all conformational clusters are shown in Supplementary Fig. 6): the GBSII oligosaccharides form compact coiled conformations (Fig. 3 A-C; left panel) while the GBSIII oligosaccharides form extended zig-zag conformations (Fig. 3 D-E; right panel) that are consistent with previous modeling (Kuttel & Ravenscroft, 2019).

All the GBSII backbones form a central 5 RU pentagonal ring, which involves the whole chain for the 6 RU molecule (37 % occupancy, Fig. 3A, chain colored grey in the inset) and the middle 5 RUs for the 9 RU (Fig. 3B, inset) and 12 RU (Fig. 3C, inset) chains. The Neu5Ac-linked Gal residues of the GBSII backbone form the corners of the pentagon. Each side of the pentagon has a Gal side chain (yellow) inside the ring (less solvent exposed) and a Neu5Ac side chain (purple) outside the ring (more solvent exposed). For the 9 and 12 RU molecules, the ends of the chain not involved in the ring (shown in green and orange in the inset box) are free to move, resulting in lower occupancy of the primary conformational clusters. The ends extend above and below the plane of the pentagonal-ring in the 9 RU molecule (33 % occupancy) and in the 12 RU molecule they interact with each other, twisting up and folding over onto the same face of the ring (35 %). This highly compressed coiled secondary structure is stabilized by hydrogen bonding (discussed in Section 3.2.1 below). The coiled conformation means that, despite a three RU increase in length between the 6 RU, 9 RU, and 12 RU, the three molecules are very similar in volume (discussed further in Section 3.3 below).

In contrast, the GBSIII oligosaccharides both form well-defined extended zig-zag conformations with high occupancy of the primary clusters: 78 % for 10 RU chain (Fig. 3D) and 70 % for the 15 RU chain (Fig. 3E). The Neu5Ac side chains (purple, Fig. 3D-E inset boxes) are exposed on the corners of the zig-zag, partially shielding the adjacent Gal residues (yellow). The longer 15 RU molecule is relatively more extended than the 10 RU molecule, which has a bend spanning RUs 7–10, resulting in a fold in the molecule that causes a more collapsed conformation (cyan, Fig. 3D inset box). A similar "U" shaped bend occurs at the corresponding position of the 15 RU molecule (cyan, Fig. 3E inset box), but the longer RU molecule does not fold as a result instead a slight bend occurs in the otherwise linear molecule.

3.2.1. Hydrogen bonding

In both GBSII and GBSIII, hydrogen bonding between the backbone and the side chains stabilizes the bends in the backbone that generate the characteristic conformations of the CPS (Fig. 4). For GBSII, hydrogen bonding occurs between Neu5Ac (purple) and the backbone *β*Glc (blue) residues (indicated by orange spheres in Fig. 4A). For GBSIII, there is more extensive hydrogen bonding between the longer Neu5Ac(2➔3)Gal side chain and the backbone *β*Glc (Fig. 4B), as previously reported (Kuttel & Ravenscroft, 2019).

Table 2
Approximate volumes (Å^3) and solvent accessible surface areas (sasa) (Å^2) for the representative frames of the primary clusters for the modeled GBSII and GBSIII molecules.

GBSII			GBSIII		
RUs	Approximate Volume (x10^4 Å^3)	Approximate SASA (x10^4 Å^2)	RUs	Approximate Volume (x10^4 Å^3)	Approximate SASA (x10^4 Å^2)
6	2.14	0.78	**10**	2.63	0.94
9	3.06	1.07	**15**	4.05	1.47
12	4.04	1.42	–	–	–

Additional hydrogen bonds between HO3 of βGlc (or GlcNAc) and neighboring O5 Gal (indicated by red spheres in Fig. 4 and in Supplementary Fig. 7) further stabilize the relative orientation of backbone residues. In GBSII, hydrogen bonds stabilize both the pentagonal corners (Fig. 4A: bond from GN to GAL^{II}) and the sides of the pentagon relative to each other (Fig. 4A: GAL^{I} to G) and are present in all RUs of the molecule (Supplementary Fig. 7 A). Similarly, in GBSIII hydrogen bonds stabilize the zig-zag bend (Fig. 4B: GN^{I} to GAL^{I}) and the relative orientation of backbone residues in the straight sections of the backbone (Fig. 4B: GAL to G). The fold seen in the 10 RU molecule (but not the 15 RU molecule), occurs in a repeat unit where the hydrogen bond from GN^{I} to GAL^{I} is absent (Supplementary Fig. 7 inset box), thereby destabilizing the zig-zag.

Through-space Nuclear Overhauser Effect (NOE) nuclear magnetic resonance (NMR) experiments for GBSII (GBSIII has been previously reported (Kuttel & Ravenscroft, 2019)) produced complex and highly overlapped spectra for which unambiguous assignments were difficult. However, the few NOE correlations that could be assigned unambiguously were consistent with the model and observed hydrogen bonds (Supplementary Section 2 and Supplementary Figs. 8–10).

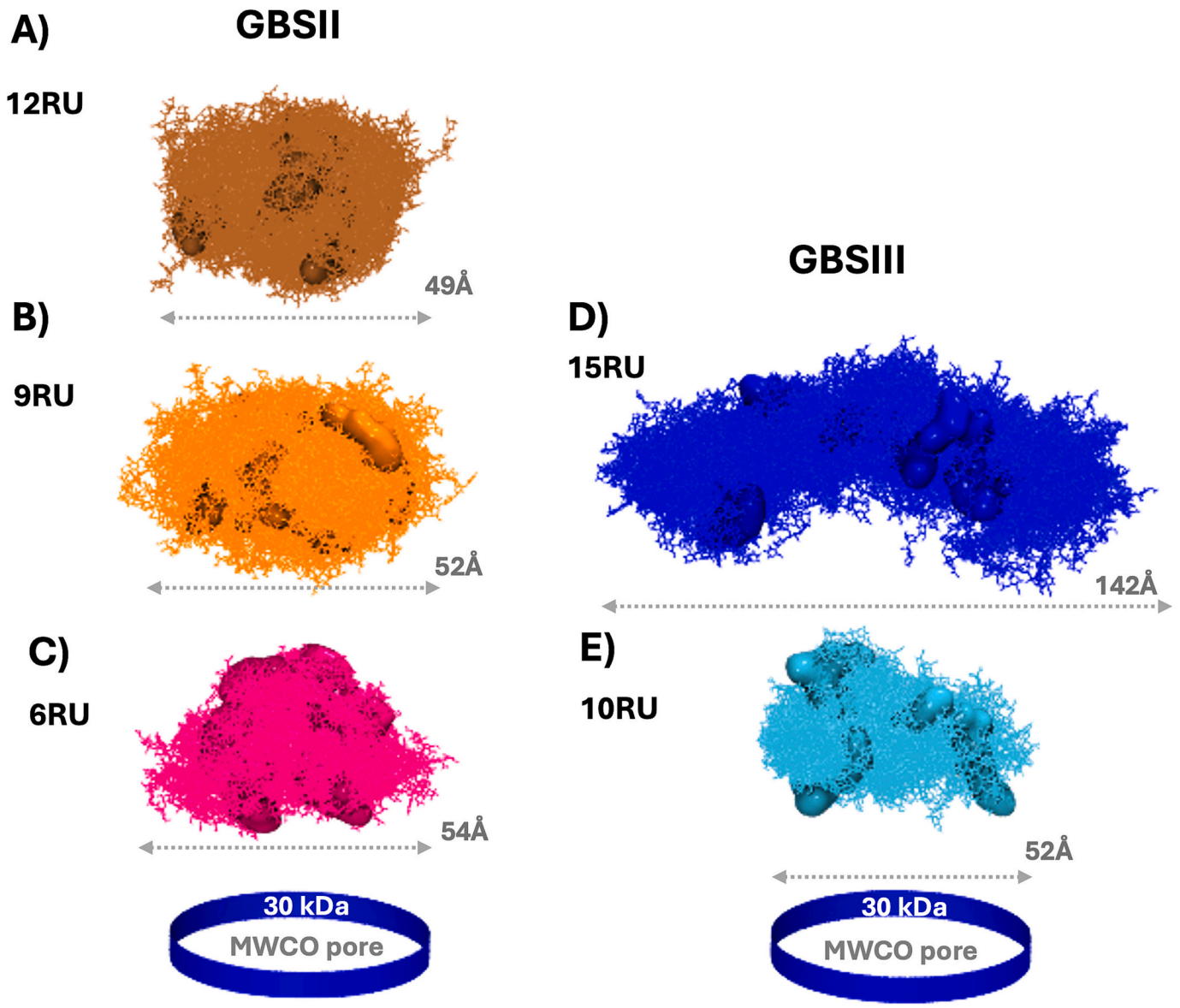

Fig. 5. The molecular footprint of the molecules indicated by overlays of trajectory frames on the molecular surface for: **A)** GBSII12 RU (brown) **B)** GBSII 9 RU (orange) **C)** GBSII 6 RU (pink) **D)** GBSIII 15 RU (dark blue) **E)** GBSIII 10 RU (light blue). For GBSII, as RU length increases, the molecular footprint decreases and becomes more globular, whereas for GBSIII the molecular footprint becomes more elongated and increases in length with increasing RU length. Blue circular rings are shown below the molecules to represent a 30 kDa MWCO filter pore illustrating how the smaller molecular footprint for GBSII molecules compared to GBSIII would preferentially allow them to fall through the pore. Molecules are labeled with their end-to-end length (Å), every 100th trajectory frame is shown.

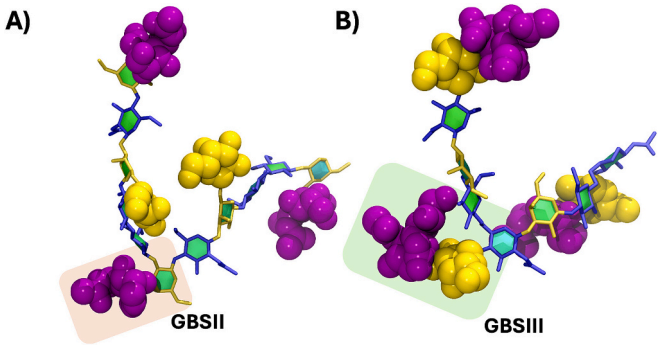

Fig. 6. Representative fragments of the modeled molecules showing differences in potential binding epitopes from: **A)** GBSII 9 RU and **B)** GBSIII 15 RU. Backbones are shown in Licorice and side chains in VDW representation. Orange or green shaded boxes indicate a common Neu5Ac(2➔3) Gal motif that differs in linkage positions and spatial orientation. Backbones are shown in Licorice and side chains in VDW representations and colors as per SNFG: blue – glucose, yellow – galactose, purple – sialic acid.

3.3. Molecular surface and volume

Filtration with molecular weight cutoff (MWCO) filters is based on the hydrodynamic volume of the molecule, with MWCO filters referenced against globular proteins. Therefore, the calculated volume and solvent accessible surface area (sasa) of the GBSII and GBSIII (Table 2) molecules provide an approximation of the relative molecular volumes and surfaces to correlate with the differing observed filtration behaviors of GBSII and GBSIII.

As expected, as the length of the molecules increases, so does the molecular volume and surface area. However, for the same backbone length, the GBSIII molecules have a greater volume and sasa than the corresponding GBSII molecules: the 10 RU GBSIII volume and sasa are 23 % and 17 % larger respectively than the 6RU GBSII; and the 15 RU GBSIII 32 % and 37 % greater than the 9 RU GBSII. This difference is illustrated by the molecular footprints shown in Fig. 5, represented by the primary conformations of the GBSII (left column) and GBSIII (right column) oligosaccharides overlaid with conformations spanning the trajectory. It is clear: firstly, that the hydrodynamic volume of GBSII decreases with increasing chain length, whereas for GBSIII it increases; and, secondly, that GBSII is considerably more globular and compressed than GBSIII. This is most apparent in the longest 12 RU GBSII molecule: simulation of this length of chain was necessary to confirm the conformational collapse. This provides a mechanistic rationale for the filtration behavior of GBSII: GBSII's smaller hydrodynamic size will cause it to preferentially slip through the pores in the MWCO filter, leading to reduced retention compared to the more elongated GBSIII.

3.4. Potential antibody binding epitopes

The lack of cross-reactivity observed between GBSII and GBSIII serotypes can be rationalized by analysis of potential antibody binding epitopes. Antibodies typically bind only up to six residues (Kabat, 1966; Nonne et al., 2024). Stretches of 2–3 RU for GBSII and GBSII (Fig. 6) show significant differences in spatial arrangement of the residues that contribute to different potential binding epitopes. The Neu5Ac side chain residues (purple spheres) have been shown to be important immune determinants critical for bacterial virulence in GBS serotypes (Heath & Feldman, 2005). Further, Neu5Ac is critical for antibody binding in GBSIII (Baker & Kasper, 1985; Carboni et al., 2017) and is solvent exposed as a potential epitope in both GBSII (Fig. 6A, orange shaded region) and GBSIII (Fig. 6B, green shaded region). For GBSII, the Neu5Ac side chains are exposed on the outside of the pentagonal ring and the Gal side chains (yellow spheres) are arranged opposite on the inside of the pentagonal ring and, hence, are less solvent exposed. In GBSIII the side chain comprises a Gal and terminal Neu5Ac and is solvent exposed on the outside of the zig-zag conformation.Although GBSII and GBSIII have a similar potential epitope Neu5Ac2➔3Gal, they have different spatial organization and arrangement of this epitope relative to the backbone. In GBSII this epitope includes a backbone linked Gal, whereas in GBSIII this epitope is entirely contained in the side chain. Further, the distance between consecutive epitopes is longer in GBSII as the backbone has additional residues.

The interaction of a 2 RU GBSIII molecule (DP2) with the a GBSIII monoclonal fragment antibody (FAb) NVS-1-19-5 (PBD code 5 m63) has been previously described (Carboni et al., 2017; Kuttel & Ravenscroft, 2019): the side chain terminal Neu5Ac is contained in a deep binding pocket and the backbone GlcNAc residue in a distal, shallower binding pocket (Fig. 7A; binding pockets indicated by stars) about 11 Å apart from each other.

We can compare how GBSII and GBSIII would (or would not) bind the GBSIII FAb to help understand their lack of cross-reactivity. A comparison of 2 RU fragments (corresponding to DP2) of GBSII and GBSIII (Fig. 7B and C) as potential binding epitopes for this FAb shows the impact of different spatial arrangements. For GBSII, the distance between Neu5Ac and GlcNAc residues in a binding configuration is ~17 Å (orange shaded boxes in Fig. 7B), compared to ~11 Å in GBSIII (green shaded boxes in Fig. 7C). Further, overlays of these potential epitopes with the antibody binding site show the poor fit of the GBSII epitope (Fig. 7B, right panel) compared to the GBSIII epitope (Fig. 7C, right panel); the GBSII side chain Neu5Ac is not contained within the deep Neu5Ac binding pocket due to it being a shorter side chain than in GBSIII and the backbone GlcNAc residue is not contained in the shallower binding pocket due to the longer GBSII backbone RU (five residues versus three in GBSIII). Thus, spatial differences in the GBSII epitope prevent high avidity binding of the GBSIII FAb and provide insight into the lack of cross-reactivity between GBSII and GBSIII.

As further validation of our modeled GBSIII 10 and 15 RU molecules, we show how the full-length chains easily align with DP2 in the antibody binding site with no antibody-CPS intersection as per the binding model described by Carboni et al. (Fig. 7D: GBSIII 10 RU – purple; 15 RU - orange) (Carboni et al., 2017). Similarly, Fig. 7E shows the alignment of a sample of the frames from the GBSIII 10 (purple) and 15 RU (orange) trajectories with the antibody. In both cases, the bulk of the CPS is in a conformation that would minimize antibody-CPS intersection especially in the case of the 10 RU molecule (purple) where the bend in the backbone creates an accessible and less hindered epitope for antibody binding with the balance of the flexible backbone held well away from the antibody over the course of the simulation.

4. Discussion

This study highlights the utility of modeling extended GBSII and GBSIII chains to gain mechanistic rationale for the anomalous filtering behavior of GBSII: despite structural similarities, GBSII adopts very compact conformations in stark contrast to the more extended GBSIII. Further, the modeling helps rationalize the absence of immunological cross-reactivity.

Selecting appropriate chain lengths is crucial in molecular modeling. While longer chains provide greater biological accuracy, they significantly increase computational cost (Cramer, 2013). Typically, we use six repeating unit (RU) simulations to study potential antibody-binding epitopes (Kuttel, 2022; Richardson et al., 2022; Richardson et al., 2023) which, in the case of GBS, would contain the minimal epitope (1–2 RU) (Carboni et al., 2017; Nonne et al., 2024). However, to elucidate the secondary structures and conformational differences causing the observed physical differences in GBSII and GBSIII, it was necessary to simulate much longer chain lengths (9 and 12 RU for GBSII or 10 and 15 RU for GBSIII).

Our simulations of 10 and 15 RU GBSIII reveal a flexible zig-zag backbone conformation with a relatively stable branch point for side

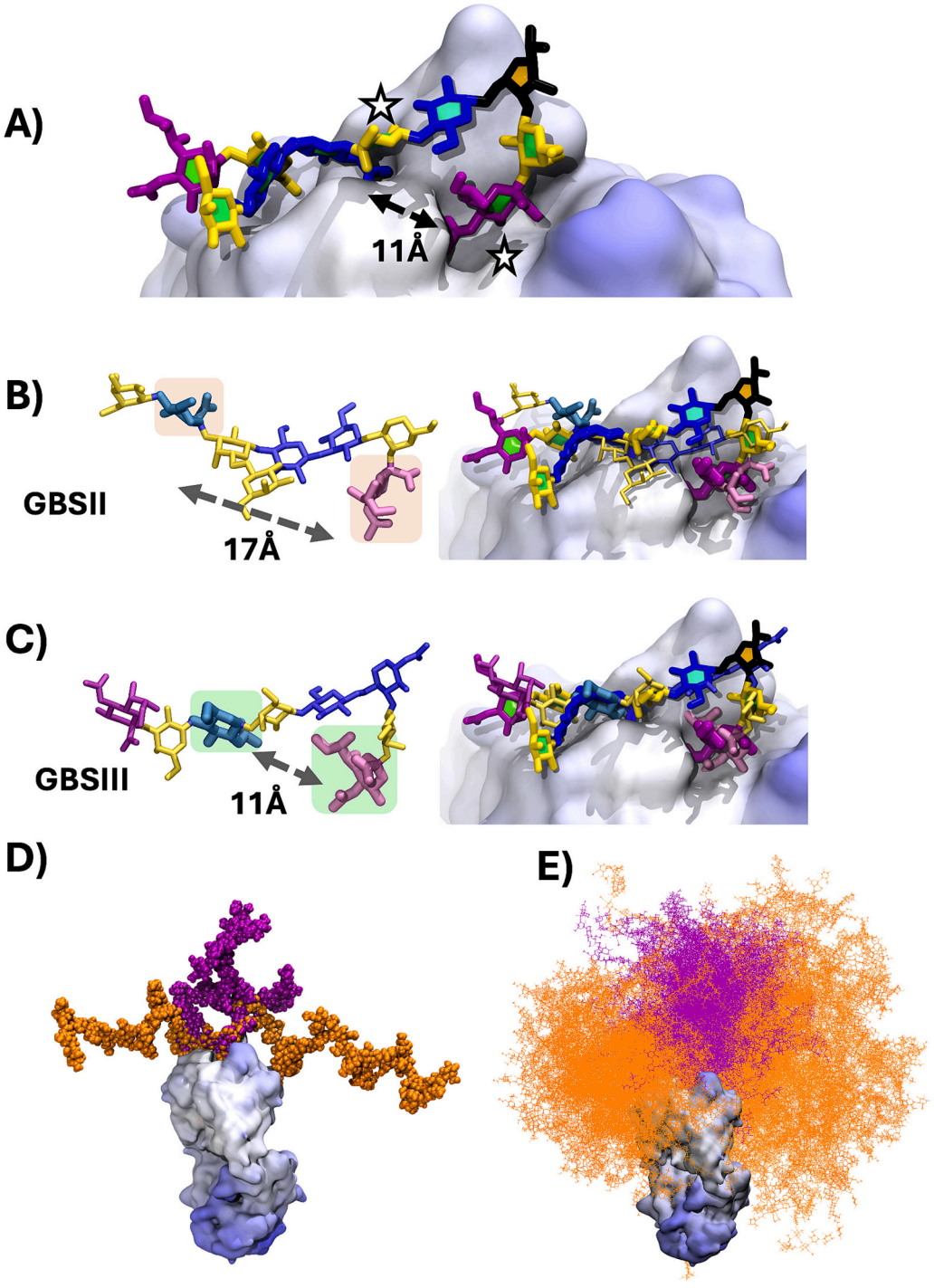

Fig. 7. A) Close-up view of the binding site from the crystal structure of rabbit monoclonal anti-PSIII NVS-1-19-5 fragment antibody (FAb) in complex with DP2 GBSIII 2 RU fragment (PDB ID: 5M63). A deep binding site for Neu5Ac (purple) and shallower pocket for GlcNAc (blue) are present (indicated by white stars) about 11 Å apart. **B)** Fragments of the GBSII 9 RU and **C)** GBSIII 15 RU molecules corresponding to the Fab-bound DP2 fragment, with the distance between the two bound residues indicated. Orange and green shaded boxes indicate a common Neu5Ac(2➔3) Gal motif that differs in linkage positions and spatial orientation. Overlays with the binding site are shown in the right panels indicating poor fit with GBSII and good fit with GBSIII. **D)** Representative frames of 10 RU (purple) and 15 RU (orange) GBSIII molecules aligned in the FAb monomer binding site showing with no intersection of the CPS and the antibody. **E)** FAb monomer with every 200th frame of the GBSIII 10 RU (purple) and 15 RU (orange) simulation trajectory aligned and overlaid in the DP2 in the binding site.

chain attachment. This aligns well with our previous modeling study of 6 RU GBSIII (Kuttel & Ravenscroft, 2019). The CPS displays increasing volume and solvent accessible surface area (sasa) as the chain length increases. Importantly, side chain Neu5Ac residues are highly solvent-exposed and accessible facilitating potential antibody binding on the outside of the backbone zig-zag.

Conversely, the corresponding 6, 9, and 12 RU of GBSII adopt collapsed, globular conformations with progressively reduced volume and sasa as chain length increases. The backbones form interesting pentagonal curves from the central RUs and are comprised of linear sides with corners bearing immunologically important Neu5Ac side chains exposed on the outside of the ring. The Gal side chains tend to arrange

inside the pentagonal ring and are less solvent exposed thus, potentially less available for antibody binding.

Polysaccharide flexibility and conformation has been shown to significantly impact ultrafiltration performance with molecular weight cutoff (MWCO) filter membranes. These membranes are typically sized based on sphere-like globular marker proteins, which have a narrow molecular weight to hydrodynamic volume relation. Previous studies have shown that recoveries of random-coil polysaccharides (pullulan) and rigid-rod polysaccharides (scleroglucan) can differ by up to 70 %, despite similar molecular weights and charges (Eder et al., 2021). It has been suggested that the higher flexibility of random-coil polysaccharides (pullulan) allows for a more compact spatial alignment and a lower effective hydrodynamic radius, reducing filtering recovery since linear shapes (e.g. rigid-rod like scleroglucan) have lower probability of entering a pore than a sphere (Vinther et al., 2012). Similarly, we find that, for the same backbone lengths, GBSII adopts more compact, pullulan-like conformations with lower calculated volumes and sasa compared to the more extended, scleroglucan-like GBSIII, indicating a lower hydrodynamic radius. We therefore expect the more globular, compact GBSII to pass more easily through a MWCO membrane than a similarly sized, but more extended and linear, GBSIII molecule. Thus, we can propose a mechanism for the physically observed differences in filtering behaviors with GBSII being poorly retained by a 30 kDa filter and GBSIII well retained. This result demonstrates the utility of molecular modeling methodologies in explaining physical and experimentally observed phenomena.

Understanding the relationship between polysaccharide length and immunogenic response is important for both understanding the minimum protective epitope and synthetic vaccine design. For GBSIII, the minimal binding epitope spans two RUs, with binding improving up to approximately 20 RUs before plateauing (Carboni & Adamo, 2020; Carboni et al., 2017; Michon et al., 2006; Zou et al., 1999). In contrast, the functional response of antibodies to GBSII CPS appears inversely correlated with polysaccharide length: glycoconjugate vaccines with ~11 RU eliciting stronger immune responses than longer chains or high molecular weight native CPS (Michon et al., 2006). These differences align with our conformational findings: GBSIII remains extended and solvent-accessible with increasing chain length, while GBSII becomes more collapsed, reducing the number of accessible, solvent exposed RUs.

The lack of cross-reactivity between GBSII and GBSIII can be explained by structural and spatial differences in potential antibody binding epitopes. The Neu5Ac and Gal residues are specific but not complete epitopes for antibody binding in GBSII and GBSIII (Carboni et al., 2017; Guttormsen et al., 2002; Jennings et al., 1981; Kasper et al., 1979; Kasper et al., 1983). While both GBSII and GBSIII share a common Neu5Ac(2➔3)Gal motif, differences in structural arrangement as well as backbone RU length lead to spatial differences that would prevent effective cross-binding. This was shown with a GBSIII specific fragment antibody which binds Neu5Ac and GlcNAc of the same RU, but has too short a distance between these binding pockets for high avidity binding to GBSII, due to the longer GBSII backbone RU. Further, the deep Neu5Ac binding pocket comfortably accommodates the two residue Neu5Ac side chain in GBSIII, but not the single residue Neu5Ac side chain of GBSII which would be too short to allow for high avidity binding. Thus, we can rationalize the lack of cross-reactive epitopes between GBSII and GBSIII molecules (Baker et al., 2003).

This work provides mechanistic insight into physically observed behavior that would be challenging to study otherwise. It also informs vaccine production strategies particularly regarding CPS purification. Future studies could extend to modeling additional GBS serotypes to better understand their structural differences and the general lack of cross-reactivity across serotypes (Carreras-Abad et al., 2020). Such insights could contribute to rational vaccine design efforts, ultimately aiming to reduce GBS disease burden and associated maternal and infant morbidity.

5. Conclusion

This molecular modeling study reveals significant conformational differences between the CPS of GBSII and GBSIII, offering a mechanistic rationale for their distinct filtering behaviors. Our findings indicate that the more compact GBSII molecules are expected to pass more easily through a smaller membrane pore than the more elongated GBSIII molecules. Further, differences in the potential antibody binding epitopes of GBSII and GBSIII explains the lack of cross-reactivity seen between these structurally related serotypes. This study underscores the value of molecular modeling in providing mechanistic understanding of physical behavior differences in polysaccharides as well as rationalizing lack of cross-reactivity, ultimately aiding our understanding of vaccine production processes and improving the quality, safety, and efficacy of vaccine products.

CRediT authorship contribution statement

Nicole I. Richardson: Writing – original draft, Visualization, Validation, Methodology, Investigation. **Francesco Berti:** Writing – review & editing, Investigation. **Neil Ravenscroft:** Writing – review & editing, Supervision, Methodology, Conceptualization. **Michelle M. Kuttel:** Writing – review & editing, Visualization, Supervision, Resources, Methodology, Funding acquisition.

Funding

This work was supported by the University of Cape Town: Industry Postdoctoral Fellowship to NIR.

Declaration of competing interest

Francesco Berti is an employee of the GSK group of companies.

Neil Ravenscroft is a consultant to PATH and BMGF on some of their vaccine development projects.

Acknowledgements

The authors thank PATH and vaccine partners for providing the GBS polysaccharide samples and Maximillian Keresztesi for performing the initial NMR analysis. Computations were performed using facilities provided by the University of Cape Town's ICTS High Performance Computing team: hpc.uct.ac.za.

Appendix A. Supplementary data

Supplementary data to this article can be found online at https://doi.org/10.1016/j.carbpol.2025.123964.

Data availability

Structure starting files (pdb and psf) as well as the representative frames for the primary conformational clusters (pdb) for each molecule modeled are included as Supplementary Information and are available with the output trajectory files (dcd) at the following repository: https://github.com/Nicole-Richardson/GBSII_GBSIII_data/tree/main.

References

Baker, C. J. (2023). Group B streptococcal vaccine — Sisyphus reconciled. *New England Journal of Medicine, 389*(3), 275–277. https://doi.org/10.1056/NEJMe2306234

Baker, C. J., & Kasper, D. L. (1985). Group B streptococcal vaccines. *Reviews of Infectious Diseases, 7*(4), 458–467. https://doi.org/10.1093/clinids/7.4.458

Baker, C. J., Rench, M. A., Fernandez, M., Paoletti, L. C., Kasper, D. L., & Edwards, M. S. (2003). Safety and immunogenicity of a bivalent group B streptococcal conjugate vaccine for serotypes II and III. *The Journal of Infectious Diseases, 188*(1), 66–73. https://doi.org/10.1086/375536

Balaeff, A. (2006, 06 March 2006). Mol_Volume - Calculate macromolecular volume. Retrieved 10 August 2024 fromhttps://www.ks.uiuc.edu/Development/MDTools/molvolume/.

Berti, F., Campisi, E., Toniolo, C., Morelli, L., Crotti, S., Rosini, R., … Torricelli, G. (2014). Structure of the type IX group B Streptococcus capsular polysaccharide and its evolutionary relationship with types V and VII. *Journal of Biological Chemistry, 289*(34), 23437–23448. https://doi.org/10.1074/jbc.M114.567974

Berti, F., Costantino, P., & Romano, M. R. (2016). *Purification of streptococcal capsular polysaccharide EP3233927A1*.

Bjerkhaug, A. U., Ramalingham, S., Mboizi, R., Le Doare, K., & Klingenberg, C. (2023). The immunogenicity and safety of group B streptococcal maternal vaccines: A systematic review. *Vaccine, 42*, 84–98. https://doi.org/10.1016/j.vaccine.2023.11.056

Burchard, W. (2003). Solubility and solution structure of cellulose derivatives. *Cellulose, 10*, 213–225. https://doi.org/10.1023/A:1025160620576

Carboni, F., & Adamo, R. (2020). Structure-based glycoconjugate vaccine design: The example of group B Streptococcus type III capsular polysaccharide. *Drug Discovery Today: Technologies, 35-36*, 23–33. https://doi.org/10.1016/j.ddtec.2020.11.003

Carboni, F., Adamo, R., Fabbrini, M., De Ricco, R., Cattaneo, V., Brogioni, B., Veggi, D., Pinto, V., Passalacqua, I., Oldrini, D., Rappuoli, R., Malito, E., Margarit, I., & y. R., & Berti, F.. (2017). Structure of a protective epitope of group B Streptococcus type III capsular polysaccharide. *Proceedings of the National Academy of Sciences, 114*(19), 5017–5022. https://doi.org/10.1073/pnas.1701885114

Carreras-Abad, C., Ramkhelawon, L., Heath, P. T., & Le Doare, K. (2020). A vaccine against group B Streptococcus: Recent advances. *Infection and Drug Resistance, 1263-1272*. https://doi.org/10.2147/IDR.S203454

Costantino, P., Norelli, F., Berti, F., Cicala, C. M., Bazzocchi, G., Fontani, S., & Olivieri, R. (2015). *Purification processes for obtaining cps from streptococci EP2235159B1*.

Cramer, C. J. (2013). What are theory, computation, and modeling?. In *Essentials of computational chemistry: Theories and models* (pp. 1–16). John Wiley & Sons.

Cross, S., Kuttel, M. M., Stone, J. E., & Gain, J. E. (2009). Visualisation of cyclic and multi-branched molecules with VMD. *Journal of Molecular Graphics and Modelling, 28*(2), 131–139. https://doi.org/10.1016/j.jmgm.2009.04.010

Dangor, Z., Seale, A. C., Baba, V., & Kwatra, G. (2023). Early-onset group B streptococcal disease in African countries and maternal vaccination strategies. *Frontiers in Public Health, 11*, 1214844. https://doi.org/10.3389/fpubh.2023.1214844

Darden, T., York, D., & Pedersen, L. (1993). Particle mesh Ewald: An N· log (N) method for Ewald sums in large systems. *The Journal of Chemical Physics, 98*(12), 10089–10092. https://doi.org/10.1063/1.464397

Defeating meningitis by 2030: a global road map. (ISBN 978–92–4-002640-7). (2021).

Del Bino, L., Calloni, I., Oldrini, D., Raso, M. M., Cuffaro, R., Ardá, A., … Adamo, R. (2019). Regioselective glycosylation strategies for the synthesis of group Ia and Ib streptococcus related glycans enable elucidating unique conformations of the capsular polysaccharides. *Chemistry–A. European Journal, 25*(71), 16277–16287.

Eder, S., Zueblin, P., Diener, M., Peydayesh, M., Boulos, S., Mezzenga, R., & Nyström, L. (2021). Effect of polysaccharide conformation on ultrafiltration separation performance. *Carbohydrate Polymers, 260*, Article 117830. https://doi.org/10.1016/j.carbpol.2021.117830

Edmond, K. M., Kortsalioudaki, C., Scott, S., Schrag, S. J., Zaidi, A. K., Cousens, S., & Heath, P. T. (2012). Group B streptococcal disease in infants aged younger than 3 months: Systematic review and meta-analysis. *The Lancet, 379*(9815), 547–556. https://doi.org/10.1016/S0140-6736(11)61651-6

Feemster, K., Hausdorff, W. P., Banniettis, N., Platt, H., Velentgas, P., Esteves-Jaramillo, A., … Buchwald, U. K. (2024). Implications of Cross-reactivity and Cross-protection for pneumococcal vaccine development. *Vaccines, 12*(9), 974. https://doi.org/10.3390/vaccines12090974

Feller, S. E., Zhang, Y., Pastor, R. W., & Brooks, B. R. (1995). Constant pressure molecular dynamics simulation: The Langevin piston method. *The Journal of Chemical Physics, 103*(11), 4613–4621.

Gonçalves, B. P., Procter, S. R., Paul, P., Chandna, J., Lewin, A., Seedat, F., … Santhanam, S. (2022). Group B streptococcus infection during pregnancy and infancy: Estimates of regional and global burden. *The Lancet Global Health, 10*(6), e807–e819. https://doi.org/10.1016/S2214-109X(22)00093-6

Grossfield, A., & Zuckerman, D. M. (2009). Quantifying uncertainty and sampling quality in biomolecular simulations. *Annual reports in computational chemistry, 5*, 23–48. https://doi.org/10.1016/S1574-1400(09)00502-7

Guttormsen, H.-K., Baker, C. J., Nahm, M. H., Paoletti, L. C., Zughaier, S. M., Edwards, M. S., & Kasper, D. L. (2002). Type III group B streptococcal polysaccharide induces antibodies that cross-react with Streptococcus pneumoniae type 14. *Infection and Immunity, 70*(4), 1724–1738. https://doi.org/10.1128/iai.70.4.1724-1738.2002

Guvench, O., & MacKerell, A. D. (2008). Comparison of protein force fields for molecular dynamics simulations. In A. Kukol (Ed.), *Vol. 443. Molecular modeling of proteins* (pp. 63–88). Humana Press. https://doi.org/10.1007/978-1-59745-177-2_4.

Guvench, O., & MacKerell, A. D., Jr. (2009). Computational evaluation of protein–small molecule binding. *Current Opinion in Structural Biology, 19*(1), 56–61. https://doi.org/10.1016/j.sbi.2008.11.009

Hayes, K., O'Halloran, F., & Cotter, L. (2020). A review of antibiotic resistance in group B Streptococcus: The story so far. *Critical Reviews in Microbiology, 46*(3), 253–269. https://doi.org/10.1080/1040841X.2020.1758626

Heath, P. T., & Feldman, R. G. (2005). Vaccination against group B streptococcus. *Expert Review of Vaccines, 4*(2), 207–218. https://doi.org/10.1586/14760584.4.2.207

Hennessey, J. P., Jr., Costantino, P., Talaga, P., Beurret, M., Ravenscroft, N., Alderson, M. R., … Frasch, C. (2018). Lessons learned and future challenges in the design and manufacture of glycoconjugate vaccines. In A. K. Prasad (Ed.), *Carbohydrate-based vaccines: From concept to clinic* (pp. 323–385). ACS Publications. https://doi.org/10.1021/bk-2018-1290.ch013.

Hoover, W. G. (1985). Canonical dynamics: Equilibrium phase-space distributions. *Physical Review A, 31*(3), 1695. https://doi.org/10.1103/PhysRevA.31.1695

Humphrey, W., Dalke, A., & Schulten, K. (1996). VMD: Visual molecular dynamics. *Journal of Molecular Graphics, 14*(1), 33–38. https://doi.org/10.1016/0263-7855(96)00018-5

Hunter, J. D. (2007). Matplotlib: A 2D graphics environment. *Computing in Science & Engineering, 9*(03), 90–95. https://doi.org/10.1109/MCSE.2007.55

Jennings, H. J., Lugowski, C., & Kasper, D. L. (1981). Conformational aspects critical to the immunospecificity of the type III group B streptococcal polysaccharide. *Biochemistry, 20*(16), 4511–4518.

Jorgensen, W. L., Chandrasekhar, J., Madura, J. D., Impey, R. W., & Klein, M. L. (1983). Comparison of simple potential functions for simulating liquid water. *The Journal of Chemical Physics, 79*(2), 926–935. https://doi.org/10.1063/1.445869

Kabat, E. A. (1966). The nature of an antigenic determinant. *The Journal of Immunology, 97*(1), 1–11. https://doi.org/10.4049/jimmunol.97.1.1

Kasper, D. L., Baker, C., Galdes, B., Katzenellenbogen, E., & Jennings, H. (1983). Immunochemical analysis and immunogenicity of the type II group B streptococcal capsular polysaccharide. *The Journal of Clinical Investigation, 72*(1), 260–269. https://doi.org/10.1172/JCI110965

Kasper, D. L., Baker, C. J., Baltimore, R. S., Crabb, J., Schiffman, G., & Jennings, H. (1979). Immunodeterminant specificity of human immunity to type III group B streptococcus. *The Journal of Experimental Medicine, 149*(2), 327–339. https://doi.org/10.1084/jem.149.2.327

Krone, M., Stone, J. E., Ertl, T., & Schulten, K. (2012). Fast visualization of Gaussian density surfaces for molecular dynamics and particle system trajectories. *EuroVis (Short Papers), 10*, 067–071. https://doi.org/10.2312/PE/EuroVisShort/EuroVisShort2012/067-071

Kuttel, M., Mao, Y., Widmalm, G., & Lundborg, M. (2011). CarbBuilder: An adjustable tool for building 3D molecular structures of carbohydrates for molecular simulation. 2011 IEEE seventh international conference on eScience,.

Kuttel, M. M. (2022). Comparative molecular modelling of capsular polysaccharide conformations in Streptococcus suis serotypes 1, 2, 1/2 and 14 identifies common epitopes for antibody binding. *Frontiers in Molecular Biosciences, 9*, Article 830854. https://doi.org/10.3389/fmolb.2022.830854

Kuttel, M. M., & Ravenscroft, N. (2019). Conformation and Cross-protection in group B Streptococcus serotype III and Streptococcus pneumoniae serotype 14: A molecular modeling study. *Pharmaceuticals, 12*(1), 28. https://doi.org/10.3390/ph12010028

Kuttel, M. M., Ståhle, J., & Widmalm, G. (2016). *CarbBuilder: software for building molecular models of complex oligo-and polysaccharide structures., 37*(22), 2098–2105. https://doi.org/10.1002/jcc.24428

Luis, G. (2012). *WMC PhysBio clustering, VMD plugin*. Available at: https://github.com/luisico/clustering (last accessed June 2025).

Lundborg, M., & Widmalm, G. (2011). Structural analysis of glycans by NMR chemical shift prediction. *Analytical Chemistry, 83*(5), 1514–1517. https://doi.org/10.1021/ac1032534

Madhi, S. A., Anderson, A. S., Absalon, J., Radley, D., Simon, R., Jongihlati, B., … v., Izu, A., Naidoo, N., Kwatra, G., Ramsamy, Y., Said, M., Jones, S., Jose, L., Fairlie, L., Barnabas, S. L., Newton, R., Munson, S.,…Jansen, K. U.. (2023). Potential for maternally administered vaccine for infant group B Streptococcus. *New England Journal of Medicine, 389*(3), 215–227. https://doi.org/10.1056/NEJMoa2116045

Mantina, M., Chamberlin, A. C., Valero, R., Cramer, C. J., & Truhlar, D. G. (2009). Consistent van der Waals radii for the whole main group. *The Journal of Physical Chemistry A, 113*(19), 5806–5812. https://doi.org/10.1021/jp8111556

Michon, F., Uitz, C., Sarkar, A., D'Ambra, A. J., Laude-Sharp, M., Moore, S., & Fusco, P. C. (2006). Group B streptococcal type II and III conjugate vaccines: Physicochemical properties that influence immunogenicity. *Clinical and Vaccine Immunology, 13*(8), 936–943. https://doi.org/10.1128/CVI.00122-06

Navarro-Torné, A., Curcio, D., Moïsi, J. C., & Jodar, L. (2021). Burden of invasive group B Streptococcus disease in non-pregnant adults: A systematic review and meta-analysis. *PLoS One, 16*(9), Article e0258030. https://doi.org/10.1371/journal.pone.0258030

Neelamegham, S., Aoki-Kinoshita, K., Bolton, E., Frank, M., Lisacek, F., Lütteke, T., … Toukach, P. (2019). Updates to the symbol nomenclature for glycans guidelines. *Glycobiology, 29*(9), 620–624. https://doi.org/10.1093/glycob/cwz045

Nonne, F., Iacono, L. D., Bertuzzi, S., Unione, L., Proietti, D., Norais, N., … Romano, M. R. (2024). A multidisciplinary structural approach to the identification of the Haemophilus influenzae type b capsular polysaccharide protective epitope. *ACS Central Science, 10*(5), 978–987. https://doi.org/10.1021/acscentsci.3c01515

Nosé, S., & Klein, M. (1983). Constant pressure molecular dynamics for molecular systems. *Molecular Physics, 50*(5), 1055–1076. https://doi.org/10.1080/00268978300102851

Phillips, J. C., Hardy, D. J., Maia, J. D., Stone, J. E., Ribeiro, J. V., Bernardi, R. C., … Jiang, W. (2020). Scalable molecular dynamics on CPU and GPU architectures with NAMD. *The Journal of Chemical Physics, 153*(4). https://doi.org/10.1063/5.0014475

Pinto, V., & Berti, F. (2014). Exploring the group B Streptococcus capsular polysaccharides: The structural diversity provides the basis for development of NMR-based identity assays. *Journal of Pharmaceutical and Biomedical Analysis, 98*, 9–15. https://doi.org/10.1016/j.jpba.2014.05.004

Procter, S. R., Gonçalves, B. P., Paul, P., Chandna, J., Seedat, F., Koukounari, A., … Jit, M. (2023). Maternal immunisation against group B Streptococcus: A global analysis of health impact and cost-effectiveness. *PLoS Medicine, 20*(3), Article e1004068. https://doi.org/10.1371/journal.pmed.1004068

Raabe, V. N., & Shane, A. L. (2019). Group B streptococcus (Streptococcus agalactiae). *Microbiology Spectrum, 7*(2). https://doi.org/10.1128/microbiolspec.gpp3-0007-2018

Richardson, N. I., Kuttel, M. M., & Ravenscroft, N. (2022). Modeling of pneumococcal serogroup 10 capsular polysaccharide molecular conformations provides insight into epitopes and observed cross-reactivity. *Frontiers in Molecular Biosciences, 9*, Article 961532. https://doi.org/10.3389/fmolb.2022.961532

Richardson, N. I., Ravenscroft, N., Arato, V., Oldrini, D., Micoli, F., & Kuttel, M. M. (2021). Conformational and immunogenicity studies of the Shigella flexneri serogroup 6 O-antigen: The effect of O-acetylation. *Vaccines, 9*(5), 432. https://doi.org/10.3390/vaccines9050432

Richardson, N. I., Ravenscroft, N., & Kuttel, M. M. (2023). Conformational comparisons of Pasteurella multocida types B and E and structurally related capsular polysaccharides. *Glycobiology, 33*(9), 745–754. https://doi.org/10.1093/glycob/cwad049

Schifferle, R. E., Jennings, H. J., Wessels, M. R., Katzenellenbogen, E., Roy, R., & Kasper, D. L. (1985). Immunochemical analysis of the types Ia and Ib group B streptococcal polysaccharides. *Journal of immunology (Baltimore, Md.: 1950), 135*(6). https://doi.org/10.4049/jimmunol.135.6.4164, 4164-4170.

Van Gunsteren, W. F., & Berendsen, H. J. (1988). A leap-frog algorithm for stochastic dynamics. *Molecular Simulation, 1*(3), 173–185. https://doi.org/10.1080/08927028808080941

Varki, A., Cummings, R. D., Aebi, M., Packer, N. H., Seeberger, P. H., Esko, J. D., … Kinoshita, T. (2015). Symbol nomenclature for graphical representations of glycans. *Glycobiology, 25*(12), 1323–1324. https://doi.org/10.1093/glycob/cwv091

Vinther, F., Pinelo, M., Brøns, M., Jonsson, G., & Meyer, A. S. (2012). Statistical modelling of the interplay between solute shape and rejection in porous membranes. *Separation and Purification Technology, 89*, 261–269. https://doi.org/10.1016/j.seppur.2012.01.032

WHO bacterial priority pathogens list. (2024). *Bacterial pathogens of public health importance to guide research, development and strategies to prevent and control antimicrobial resistance*. Geneva, ISBN 978-92-4-009346-1.

Zou, W., Mackenzie, R., Thérien, L., Hirama, T., Yang, Q., Gidney, M. A., & Jennings, H. J. (1999). Conformational epitope of the type III group B Streptococcus capsular polysaccharide. *The Journal of Immunology, 163*(2), 820–825. https://doi.org/10.4049/jimmunol.163.2.820